# Enhanced Second Harmonic Generation in Double-Resonance Colloidal Metasurfaces

Yuan Zeng<sup>1,3</sup>,<sup>‡</sup> Haoliang Qian<sup>2</sup>, <sup>‡</sup>Matthew J. Rozin<sup>1,3</sup>,<sup>‡</sup> Zhaowei Liu<sup>2,3</sup> and Andrea R. Tao<sup>1,3</sup>\*

<sup>1</sup>Department of NanoEngineering, University of California, San Diego, 9500 Gilman Drive MC 0448, La Jolla, California 92093-0448

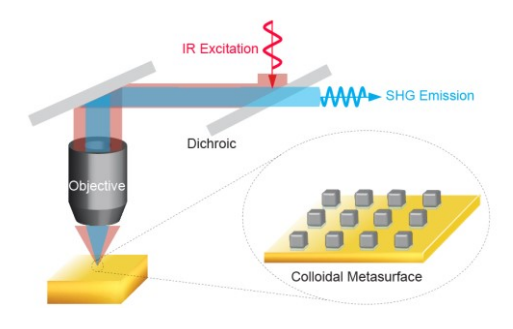
<sup>2</sup>Department of Electrical and Computer Engineering, University of California, San Diego, 9500 Gilman Drive, La Jolla, California 92093

<sup>3</sup>Materials Science and Engineering, University of California, San Diego, 9500 Gilman Drive, La Jolla, California 92093

<sup>‡</sup>These authors contributed equally to this work.

\*Email: atao@eng.ucsd.edu

## **Table of Contents Graphic:**



#### **Abstract:**

A key challenge for optical circuits is the ability to integrate nonlinear optical signal processing components such as optical modulators and frequency mixers at the chipscale. Optical antennas that focus light into nanoscale volumes can be utilized to shrink the footprint and increase the efficiency of these components. Multi-resonant antennas

that enhance both optical absorption and emission process have been recently demonstrated to enable efficient nonlinear frequency conversion at the nanoscale and are promising as structures for second harmonic generation (SHG) and upconversion. Here, we demonstrate the ability of colloidal metasurfaces fabricated by self-assembly as on-chip platforms for enhanced SHG. These metasurfaces exhibit high spatial overlap of multiple surface plasmon modes whose frequencies can be independently tuned through appropriate design of colloidal and metasurface geometries. We demonstrate that these bottom-up structures rival lithographic nonlinear optical

**Keywords:** plasmonics, metasurface, nonlinear optics, second harmonic generation

antennas in SHG efficiency, suggesting the potential for these colloidal metasurfaces

in integrated on-chip architectures.

Metallic nanostructures that support surface plasmons have been demonstrated to exhibit a wide range of nonlinear optical phenomena, 1,2 including enhanced second harmonic generation (SHG).3-5 SHG is a nonlinear wave-mixing process where two incident photons at the same fundamental wavelength ( $\lambda_{FW}$ ) combine to produce a single, higher energy photon at the second harmonic ( $\lambda_{SH} = \lambda_{FW}/2$ ) wavelength. In bulk materials that possess a large nonlinear susceptibility<sup>6</sup> ( $\chi^2$ ) such as β-barium borate and lithium niobate, SHG stems from light-matter interactions with a non-centrosymmetric crystal lattice. SHG is also supported by under-coordinated surface structures due to centrosymmetric break-down.<sup>7-11</sup> A major drawback with using surface-generated SHG, however, is a reduced nonlinear interaction length. Enhanced SHG overcomes this by taking advantage of metal surfaces that support the excitation of surface plasmon resonances (SPRs)<sup>12,13</sup> that can serve to enhance the near-field intensity<sup>14-16</sup> at either the fundamental or the second harmonic wavelengths.<sup>2,17,18</sup> However, it is difficult to match both optical excitation and emission by a structure that exhibits only a single plasmon resonance.

Double resonance nanostructures can be designed to support two different types of optical modes (e.g. a Fabry-Perot-like resonance mode and a SPR mode), <sup>19</sup> similar types of resonance modes with different polarizations, <sup>20</sup> two separate optical components that each supports a resonance mode, <sup>17,21–23</sup> or multi-resonances structure with either multiple components or branches. <sup>24–29</sup> The ability of these double resonance structures to maximize re-emission into the far-field is highly promising for the development of nonlinear light sources. However, the majority of these designs

require components that possess complex nanostructured architectures and precise control of the resonance frequencies, which determined by the size, 30 shape 31,32 and orientation 33 of metal nanostructures. As a result, nanostructured metasurfaces supporting SHG have predominantly relied on direct-write or lithography-based nanofabrication techniques, 17,19,34–36 limiting the ability to generate large-scale arrays for light emission. While suitable for building proof-of-concept structures, such fabrication processes are not amenable to nanomanufacturing considerations such as scalability, throughput, and cost.

Plasmonic metasurfaces have the potential to serve as effective platforms for enhanced SHG because they can be designed to exhibit a double resonance effect, with near-field enhancement occurring at both the fundamental and the second harmonic wavelengths. Here, we present a highly scalable, bottom-up approach to fabricating plasmonic metasurfaces for SHG and light emission. Colloidal nanocrystals assembled into periodic arrays serve as the foundation for ultrathin nonlinear optical metasurfaces that absorb in the near-infrared (IR) and emit in the visible. We observe SHG from a nanocube-on-metal structure similar to those first reported by Moreau *et al.*<sup>37</sup> Rozin *et al.* previously demonstrated that colloidal metasurfaces are capable of supporting multiple, spectrally separated but spatially overlapping plasmon resonances that induce strongly enhanced optical fields.<sup>38</sup> Such colloidal metasurfaces are particularly advantageous for enhanced SHG platforms because the parameters that affect field enhancement at the fundamental and second harmonic frequencies can be independently tuned.

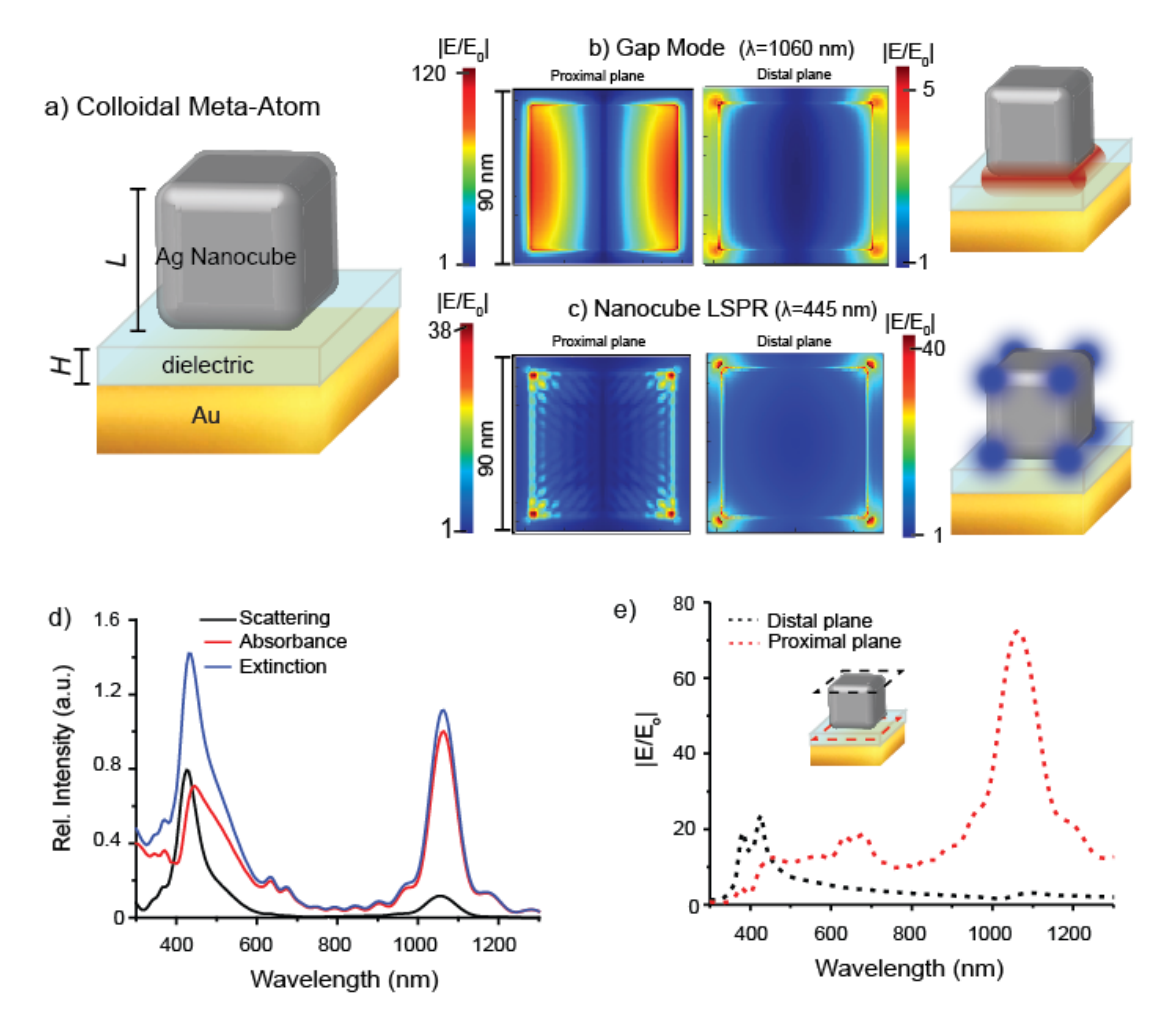


Figure 1 | Schematic and simulated Metasurface Near-Field Distributions: (a) schematic of single metaatom (90 nm cube, 10 nm radius of curvature on the corners, 3 nm dielectric layer), L is cube size and H is gap height, (b) Electric field distributions on distal plane, proximal plane, and schematic of hotspots at fundamental wavelengths (c) Electric field distributions on distal plane, proximal plane, and schematic of hotspots at second harmonic wavelengths. (d) Far-field scattering, absorbance, and calculated extinction spectra for the metasurface. (e) Local electric field intensity in the cavity (proximal) and on the AgNC top surface (distal plane) as a function of incident wavelength, inset is schematic of distal plane and proximal plane.

#### **RESULTS AND DISCUSSION**

A schematic of the metasurface geometry is shown in Figure 1a. Ag nanocubes deposited onto a metal backplane forms a metal-dielectric-metal interface that serves as the structural repeat unit, or meta-atom, of the SHG metasurface. Near-field

enhancement at the fundamental frequency is largely dictated by the thickness of the polymer space layer due to a gap mode that results from capacitive coupling between the nanocube and the Au backplane. This gap mode (Figure 1b) is largely dependent on both spacer layer thickness (which determines gap height) and cube size (which determines gap size). Field enhancement at the second harmonic frequency stems from a localized surface plasmon resonance (LSPR) associated with the Ag nanocube (Figure 1c), and is thus primarily dictated by the size of the Ag cube. This cube mode is highly dependent on cube size, but independent on spacer layer thickness. Thus, control over the structural parameters of the colloidal metasurface allow for orthogonal control over near-field enhancement at the fundamental and second harmonic frequencies.

First, we carried out full–wave electrodynamic simulations (Lumerical FDTD Solutions) to investigate how the LSPRs of the nanocube and coupled nanocube-film architecture influence SHG enhancement. The local electric-field enhancement ( $|E/E_0|$ ) distribution for a cross-section located in the nanocube-film gap, 0.5 nm below Ag nanocube bottom surface (proximal plane) is shown in Figure 1b,c. Figure 1d plots the simulated far-field scattering (black), absorbance (red), and the calculated extinction (blue) of the metasurface. The fundamental gap mode ( $\lambda$ =1060 nm) is a source of strong optical absorption and moderate scattering. Absorptions associated with confinement of the gap mode are observed at the edges of the nanocube, and are present in the simulated absorbance as oscillations in the absorbance intensity at wavelengths just above and below the fundamental mode. The absorption and

scattering peaks located between 400 nm to 700 nm in the simulated spectra are consistent with "isolated" LSPR modes of the Ag nanocube.<sup>39</sup> The broad feature at  $\lambda$ =500 nm corresponds to the first order dipole mode of the Ag nanocube, whereas the peak located near  $\lambda$ =420 nm originates from the quadrupole and other higher-order LSPRs.<sup>40</sup> However, the field enhancement induced by the quadrupole mode is dominant over the enhancement induced by dipole modes at the SHG wavelength.<sup>41</sup>The field enhancement distribution for a cross-section taken just above (0.5 nm) the top surface of the Ag nanocube (distal plane) and a cross-section taken inside the gap (proximal plane) is shown in Figure 1e. Thus, the nanocube metasurface exhibits a clear double SPR resonance: the gap mode responsible for enhanced absorption, and the nanocube LSPR responsible for emission. From the simulation of near-field distribution,

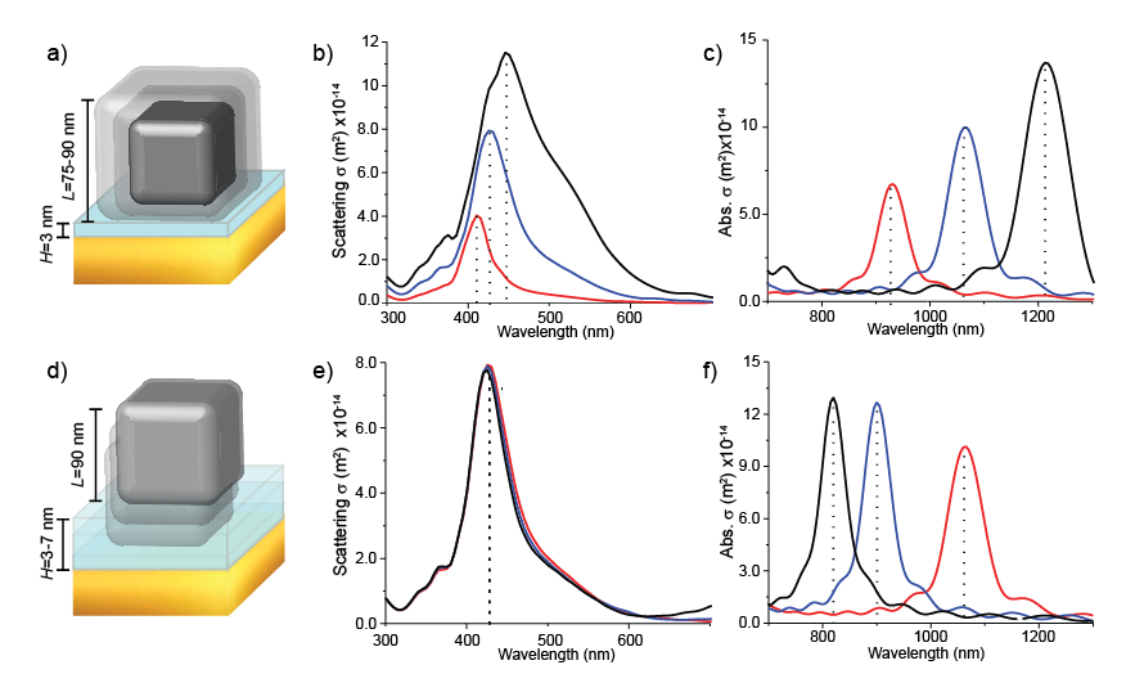


Figure 2 | Simulation, dependence of gap height and cube size: (a) Schematic of Meta-atom made by different size of cube. (b)(c) Scattering and absorption Cross-section of metasurfaces with constant (3 nm) gap size and varied cube size (Red is 75 nm, blue is 90 nm, black is 105 nm). (d) Schematic of Meta-atom made by different thickness of dielectric layer. (e, f) Scattering and absorption Cross-section of metasurfaces with constant (90 nm) cube size and varied gap size (red is= 3 nm, blue = 5 nm, black = 7 nm).

we assigned the gap mode at the fundamental wavelength as a dipole mode that stems from coupling between the Ag nanocube and Au substrate. Thus, field enhancement is consistent with SHG selection rules, 42,43 where the excitation of a SH quadrupole mode results from combined photons that stem from a dipole mode at the fundamental wavelength. 44 The spatial mode overlap that occurs inside the metasurface gap between the fundamental mode and SH mode is likely a major contributor to increasing the efficiency of the SHG process. 20

To investigate whether these two resonances can be independently tuned, we used FDTD simulations to investigate metasurface dependence on nanocube size and gap height. Figure 2 shows the resulting NIR absorption and visible scattering spectra obtained for three colloidal metasurfaces composed of: (i) different cube sizes a constant gap of H= 3 nm; and (ii) different gap heights and a constant cube edge length L=90 nm. The strong scattering peak in the visible range red-shifts significantly with increasing nanocube size, from  $\lambda$ = 410 nm for L=75 nm to  $\lambda$ = 448 nm for L=105 nm. However, optical scattering remains constant at  $\lambda$ =428 nm for all three gap heights, confirming that field enhancement near  $\lambda_{SH}$  is completely independent of H. The strong NIR absorption response is dependent on both cube size and gap height. For increasing cube size from L=75 nm to L=105 nm, the absorption peak red-shifts by 286 nm due to an increase in the optical cavity size. For increasing gap height from H=3 nm to H=7 nm, the absorption peak blue-shifts 243 nm due to weaker coupling between the nanocube and Au substrate.

To fabricate the metasurfaces, colloidal Ag nanocubes were synthesized

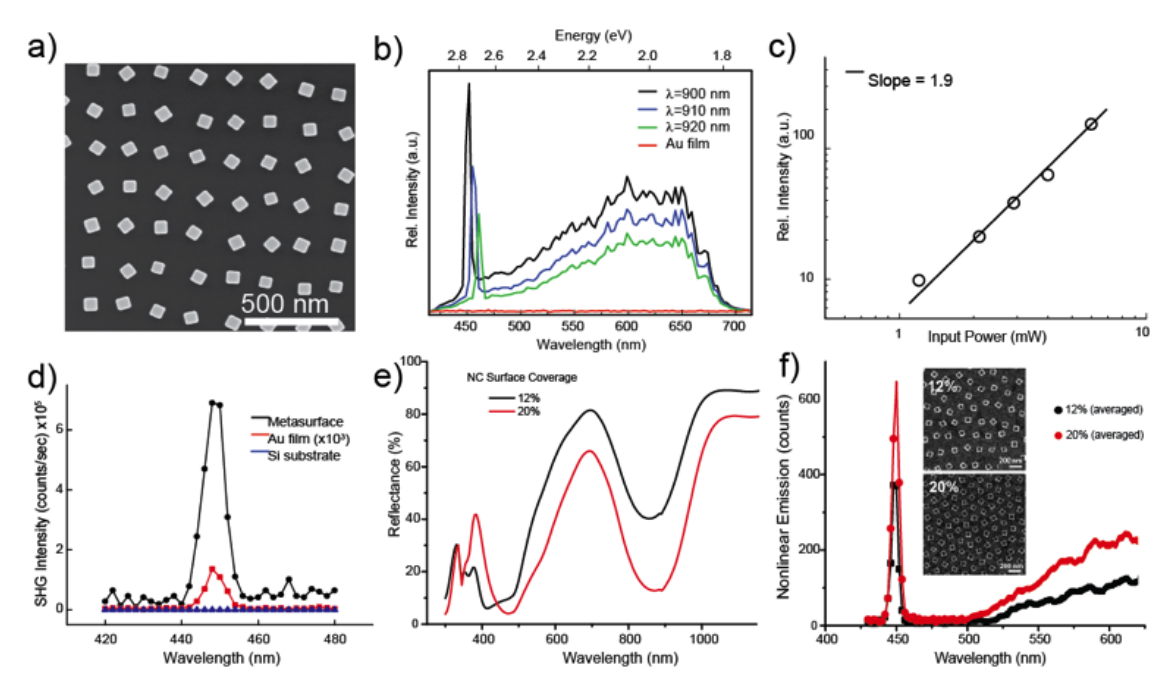


Figure 3 | Wavelength, Power and Density Dependence of Metasurface Second Harmonic Generation (a) SEM image of nanocube metasurface displaying well-spaced NC array. (b) Nonlinear emission spectra from a colloidal metasurface with a fundamental gap mode at 900 nm showing  $\lambda_{FW}$ -dependent SHG. (Corresponding reflectance spectra in Supporting Info S1) (c) SHG power dependence, showing SHG is a 2<sup>nd</sup>-order NLO process. (d) Metasurface second harmonic enhancement factor. (e) Reflectance spectra of Ag nanocube metasurfaces. (f) Nonlinear emission spectra (measured with Picosecond Photon Detection Series). Showing SHG at  $\lambda_{SH}$ =450 nm, inset is SEM images of two metasurfaces with different density. (a-c),(d-f) used two different batches of metasurfaces

according to a modified polyol reaction, described in detail elsewhere<sup>45</sup> and deposited onto a supported 50-nm Au film using Langmuir-Blodgett deposition.<sup>46</sup> (Details in Methods Section) Each nanocube is encapsulated in a thin (<2 nm) polymer shell, providing a nanoscale spacer layer that insulates the Ag nanocube from the underlying Au film. Figure 3a shows a (top-down) SEM image of a metasurface fabricated with nanocubes possessing an average edge length of 89±4 nm. The nanocube array has an average nanocube center-to-center spacing of 224±45 nm, and a nanocube purity of >98% (particle defect rate of <2%). Nanocube density and spacing can be controlled during the deposition process. A typical nonlinear optical emission spectrum for the

nanocube metasurface is shown in Figure 3b (black), excited with a scanning, normal incidence pulse train at λ<sub>FW</sub>=900 nm. During excitation at the fundamental wavelength, light-matter interactions of the plasmonic structure (at the gap mode resonance) can convert the far-field Exv component of the normal incident light to a near-field Ez component.<sup>47</sup> Plasmon excitation also promotes the interaction of the near-field with the zzz component of the second-order susceptibility tensor, which is strongly localized near the bottom facet of the AgNCs (inside the metasurface gap). Owing to the surface centrosymmetry broken at these metasurface junctions<sup>48</sup> along the z-direction, only the zzz component of the second-order susceptibility tensor is non-vanishing. Therefore, a significant near-field z-polarized coherent SHG response can be generated inside the particle-substrate gaps. The narrow SHG peak is prominent in the emission spectrum at precisely  $\lambda_{SH}$ =450 nm. The other prominent feature is the expansive range of cathedral-like peaks throughout the visible spectrum from 450 nm to 700 nm, which we attribute to multi-photon photoluminescence; their investigation is outside the primary scope of the present work and has been reported elsewhere. 49 For comparison, the nonlinear emission from a pristine Au thin-film (sans nanocubes) is shown with an identical illumination configuration, revealing a relatively flat and featureless spectrum (Figure 3b red).

The nonlinear emission spectra were also recorded for optical excitation at  $\lambda_{FW}$  = 900, 910, and 920 nm (Figure 3b). Each spectrum exhibits a narrow second harmonic peak (FWHM<6 nm) whose position follows a strict  $\lambda_{FW}/2$  dependence. Unlike this SHG peak, the broad signal attributed to multiphoton emission does not exhibit a spectral

shift with varying incident wavelengths. Figure 3c shows a log-log plot of the intensity of the second harmonic peak with respect to the input power for excitation at  $\lambda_{FW}$ =900 nm. Peak intensity was found to increase with a nonlinearity order of approximately 1.9, confirms the optical signal we measured originate from second order nonlinear process.

In order to compare the performance of our colloidal metasurface to other SPR-based SHG platforms, 19 we calculated the SHG enhancement factor (EF). Here, we define the SHG EF as the ratio of metasurface SHG power ( $P_{MS}$ ) to the SHG power of a pristine Au thin-film  $(P_{Au})$ , consistent with other studies.<sup>50</sup> Figure 3d plots the SHG emission intensity for both the colloidal metasurface, a 75 nm Au thin-film, and a 500 µm-thick Si substrate, normalized to accommodate for pump power. Here, the metasurface was fabricated with Ag nanocubes (average size=87.5 ± 3.8 nm) deposited at a surface density of 12.1%, and onto an underlying Au thin-film that is 75 nm thick. For an excitation power of 3.80 mW at  $\lambda_{FW}$ =900 nm, we measured the power of the SHG signal to be  $P_{MS} = 2.20 \times 10^{-13}$  W. Because the unenhanced SHG signal from the bare Au film is much weaker, a higher pump power was required to detect the SHG. Using an excitation power of 264.75 mW at λ<sub>FW</sub>=900 nm, we measured the SHG power from the Au film to be  $P_{Au} = 7.00 \times 10^{-14} \text{ W}$  (equivalent to  $1.45 \times 10^{-17} \text{ W}$  at 3.80mW incident power). This gives a metasurface SHG enhancement factor of EF<sub>MS</sub> = 1.52×104. In addition, we did a comparison with AgNCs on a bare Si substrate. Since there is no coupling between the AgNCs and Si, this structure serves as a single resonance structure that only exhibits a nanocube mode resonance and field enhancement at the

SHG emission wavelength. As a result, the SHG efficiency of the colloidal AgNC metasurface fabricated on Au (double resonance structure) is one order of magnitude higher than AgNCs on silicon (single resonance structure). (Supporting Information S2)"

We then compared the SHG efficiencies of two colloidal metasurfaces fabricated with different nanocube densities (12% and 20%) and all other parameters the same. Figure 3e shows their near-normal specular reflectance spectra. The large dip in reflectance centered at 875 nm corresponds to the fundamental gap resonance. The spectral positions of the fundamental gap mode for both metasurfaces are similar, indicating that there is minimal interaction between the Ag nanocubes in-plane and that both metasurfaces operate within the weak interparticle coupling limit. The only significant difference between the far-field response of each metasurface is the marked decrease in reflectance for the higher nanocube density. To calculate the SHG efficiency of each metasurface, we define efficiency as the ratio of the fundamental beam power to the metasurface SHG power:

$$\eta_{SHG} = \frac{P_{FW}}{P_{MS}}$$

For a colloidal metasurface with a 12% nanocube density excited with  $P_{FW} = 3.80 \times 10^{-3}$  W, we measured SHG efficiency to be  $\eta_{SHG} = (4.87 \pm 0.28) \times 10^{-11}$ , whereas for the 20% density metasurface the efficiency is  $\eta_{SHG} = (8.29 \pm 1.23) \times 10^{-11}$ . This 67% increase in the density of meta-atoms covering the surface leads to a 70% increase in SHG efficiency (Figure 3f), indicates the far-field emission we collected is incoherent SHG. During the emission process, the near-field z-polarized coherent SHG response cannot propagate along z-direction. However, owing to the plasmonic resonance at the SHG frequency this

coherent near-field z-polarized SHG will be converted to xy-plane polarization, then dephased and diffusely scattered through plasmonic cube mode resonance and/or light-matter interaction with nearby junctions<sup>51</sup>.

The highest efficiencies we measured were  $\eta_{SHG}$ =5.36×10-9 (Supporting information, S3) with 15.6 GW/cm² peak excitation intensity ( $\lambda_{FW}$ =800 nm, 0.2 s dwell time) and  $\eta_{SHG}$ =1.2×10-9 from the same metasurface with a longer 1 s dwell time. This decrease in efficiency indicates some materials degradation of the colloidal metasurface under extended laser illumination, potentially from either oxidation of Ag or nanocrystal reshaping due to photothermal effects. $^{52-54}$  In comparison, previous reports for bowtie apertures made by lithography exhibit  $\eta_{SHG}$ =6.33×10-9 under 0.8 GW/cm²,  $^{19}$  and comparably  $\eta_{SHG}$ =1.23×10-8 under 1.61 GW/cm² for ultrasmooth antennas. $^{20}$  While our colloidal metasurfaces exhibit lower SHG emission efficiencies, they possess much larger device areas with the potential for high meta-atom densities and wafer-scale fabrication. (See Supporting Information, S4 for a detailed comparison)

Tunability of the colloidal metasurface structure also enables further investigation of the double resonance effect. SHG enhancement is proportional to  $f(\lambda_{SH})^2 \cdot f(\lambda_{FW})^4$  where f is field strength.<sup>55</sup> Thus, the near-field enhancement at  $\lambda_{FW}$  is expected to dominate the observed SHG signal in our double-resonance structure. In a double-resonance structure, energy transfer from mode coupling ( $\eta_{rad}$ ) has also been shown to be a crucial factor in determining SHG efficiency.<sup>21</sup> To investigate the relative importance of near-field enhancement versus mode coupling, we fabricated two colloidal metasurfaces that exhibit the same nanocube LSPR modes but possess

different gap resonance wavelengths at  $\lambda$ =890 nm (labeled M890) and  $\lambda$ =1020 nm (labeled M1020).

Figure 4a,b shows the SHG excitation spectrum, which is a plot of the SHG intensity for varying fundamental excitation wavelengths between  $\lambda_{FW}$ =750–1050 nm. Data points were obtained in 50 nm increments and normalized to the incident intensity (10 GW/ cm<sup>2</sup>) (Supporting Information S5) and detector efficiency. The data points are fit with two overlapped Gaussian functions (Supporting Information S6) to identify SHG maxima. In Figure 4a, a maximum in SHG signal intensity for M890 is obtained at  $\lambda_{FW}$ =815 nm excitation, with a secondary SHG peak obtained at  $\lambda_{FW}$ =884 nm and a weak but non-zero SHG signal at  $\lambda_{FW}$ >1000 nm. Figure 4b, shows the SHG excitation scan for M1020, where a peak in SHG emission occurs at  $\lambda_{FW}$ =1029 nm, another peak located at λ<sub>FW</sub>=875 nm. Figure 4c,d shows the reflectance and absorbance for M890 and M1020, respectively. For M890, the optical resonances of the metasurface are designed to possess good overlap with  $\lambda_{FW}$  and  $\lambda_{SH}$ . For M1020, the LSPR modes of the metasurface are designed to possess poor overlap with either  $\lambda_{FW}$  or  $\lambda_{SH}$ . Figure 4e,f shows the expected SHG enhancement factors and radiation efficiencies for each metasurface. Experimental absorbance and reflectance spectra in Figure 4c,d were used to calculate the relative SHG enhancement factor  $f(\lambda_{SH})^2 \cdot f(\lambda_{FW})^4$  (Supporting Information S7). To validate these results, we performed Finite Element Method simulations to obtain the wavelength dependent radiation efficiency (blue line). These results were obtained by adding 28 dipoles sources at the hotspots inside gap (Supporting Information S8), this radiation efficiency corresponds to conversion of near-field SHG to far-field SHG. The radiation efficiency includes several factors, including coupling between the near-field SHG quadrupole mode and the far-field SHG dipole mode.

For M890 (Figure 4e), the SHG enhancement factor peak (black) at  $\lambda_{FW}$ =825

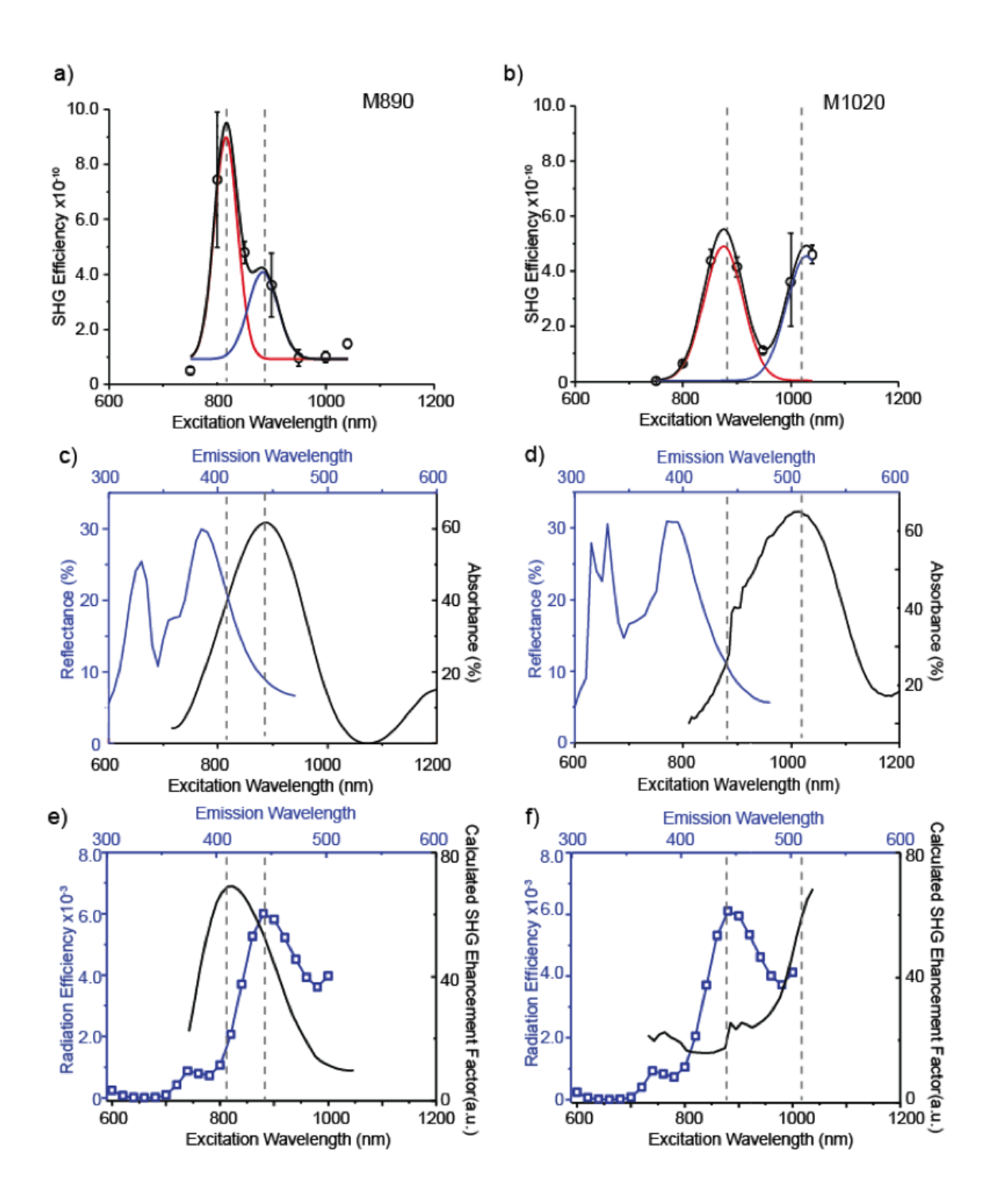


Figure 4 Linear and nonlinear optical metasurface response. Excitation wavelength dependent SHG efficiency of M890 (a) and M1020 (b), respectively, black dots are measured data points, red and blue curve are Gaussian function curve fitting. All SHG efficiency data is normalized to excitation intensity of 10 GW/cm<sup>2</sup>. Experimental reflectance and absorbance spectra for metasurfaces with fundamental gap-modes centered at 890 nm (c), and 1020 nm (d). blue curve is reflectance measurement at emission wavelength (top axis) and black curve is absorption measurement at excitation wavelength (bottom axis). Wavelength dependent radiation efficiency (blue curve) and calculated enhancement  $f(\lambda_{SH})^2 \cdot f(\lambda_{FW})^4$  (black curve) of M890 (e) and M1020 (f), respectively.

nm is consistent with strong SHG efficiency peak at  $\lambda_{FW}$ =815 nm, and the radiation efficiency peak (blue) at  $\lambda_{FW}$ =880 nm is consistent with the secondary SHG efficiency peak at 884 nm. For M1020 (Figure 4f), the SHG enhancement factor peak (black) at 1040 nm is consistent with peak in SHG emission (black) at  $\lambda_{FW}$ =1029 nm, and the maximum radiation efficiency (blue) at  $\lambda_{FW}$ =880 nm is consistent with another SHG efficiency peak at  $\lambda_{FW}$ =875 nm. To confirm the peak identification and analysis, we fabricate another metasurface with 920 nm gap mode resonance (M920) and perform excitation scan with 25 nm data interval (Supporting Information S9). Our experimental data shows M920 has two SHG efficiency peaks, one peak at 825 nm consists with enhancement factor peak, another peak at 875 nm consists with radiation efficiency peak, and both peak can be fitted with gaussian function. As a result, we find that SHG is proportional to both SHG enhancement factor and radiation efficiency ( $f(\lambda_{SH})^2 \cdot f(\lambda_{FW})^4 \cdot \eta_{Fad}$ ).

#### **CONCLUSIONS**

Overall, this work demonstrates the scalable fabrication of colloidal metasurfaces for enhanced SHG platforms utilizing a double resonance structure. We use these platforms to explore the mechanism for enhanced SHG, and determine that both near field enhancement and mode coupling are critical parameters. By tuning meta-atom size, density, and arrangement, the field enhancement associated with both nonlinear absorption and linear scattering processes can be precisely controlled. Given the ability to synthesize metal nanocrystal with a wide variety of shapes and

materials, it may be possible to greatly increase SHG efficiencies of these platforms and extend SPR-based enhancement to other nonlinear optical conversion processes. The tunability of the colloidal device structure also provides a convenient strategy for designing SHG platforms with different working frequencies, with the potential for creating hybrid structures with multiple working frequencies on a single platform. Also, since the macroscopic pattern of our metasurface is aperiodic, the far-field SHG signal we measured is incoherent. Future experiments to resolve this incoherence could potentially study periodic colloidal metasurfaces fabricated by using surface functionalized AgNCs, or optical measurements using oblique angle excitation and collection. These experiments may show the possibility of generating far-field coherent SHG from a colloidal metasurface, which has potential to further increase SHG efficiency of wafer scale metasurface by orders of magnitude.

#### **METHODS**

Gold Substrate Fabrication. Au Substrates are fabricated through Sputtering (using Denton Discovery 18 Sputter System). 500 um thick, 1 cm by 1 cm size glass substrates were washed with ethanol, piranha solution, DI water and dryied with Nitrogen stream. The sputtering RF bias is used to clean the substrate for 40 seconds, and follows with Cr (400 W, 5 second) and Au film (300 W, 115 second) sputtering with the Ar gas pressure as 2.4 mTorr.

**AgNC Synthesis**. AgNCs are synthesized via a polyol synthesis described before<sup>45,56</sup>. We add CuCl<sub>2</sub>, AgNO<sub>3</sub>, 1,5-pentanediol in a glass vial and dissolve through

sonication. In a separate glass vial, we dissolved PVP (MW=55000) in 1,5-pentanediol. Then we add 10mL 1,5-pentanediol in a 50mL Round Bottom Flask, heat up to 193 degrees and inject the precursors into the hot solution. The synthesized AgNCs are vaccum-filtered (using 650 nm, 450 nm and 220 nm pore size Millipore Durapore membranes) to reduce the polydispersity. The filtered AgNCs are centrifuged in ethanol to remove excess PVP and re-dispersed in 15 mL ethanol for later using.

Metasurface Fabrication. Take 3 mL AgNCs (stored in ethanol), add 17 mL ethanol and centrifuge at 3400 RPMs for 15 minutes, re-disperse in 10 mL ethanol and centrifuge at 3400 RPMs for 15 minutes. Then add 1 mL CHCl<sub>3</sub> and sonicate to fully dispersed. Fill a glass petri dish with DI water, add AgNCs (in CHCl<sub>3</sub>) drop by drop to the petri dish. More drops added, the higher AgNCs film density we achieved. After making the AgNCs film, wait about 1 hour and transfer the AgNCs film to the Au substrates by simply dipping into the petri dish.

SHG Measurement With Confocal Microscope (Figure 3b, c). We use back-scattering mode of Leica SP5 Confocal/MultiPhoton System (Leica Upright Microscope; 0.75NA 20x dry objective; Leica GaAsP hybrid PMT detector). A tunable Ti-Sapphire laser was used as the excitation source with approximately 100 femtosecond pulse width, 80 MHz repetition rate, and tunable emission from 690–1040 nm.

SHG Measurement With Picosecond Photon Detection Series. We use picosecond photon detection series for all SHG measurements except for Figure 3b,c because it has well-calibrated counts to photon number conversion efficiency, for accurate measurement of SHG emission power. The excitation laser source is MaiTai

HP (100fs Pulse Width and 80MHz Repetition Rate, 690 nm to 1040 nm tunable wavelength); the objective lens is 20x with 0.45NA; microscope is Olympus IX81; detector is Horiba PM, Picosecond Photon Detection Series.

We chose excitation wavelength from 750 nm to 1040 nm, with 50 nm increment (with the exception of a 40 nm increment between last two data point). For each individual measurement, excitation wavelength and laser power are constant, we carried out an emission scan using a monochromator starting at 300 nm and with a 2 nm bandwidth, 2 nm increments, and a 1 second dwell time (unless otherwise noted). Then we calculated the total counts from  $(\frac{\lambda_{Excitation}}{2} - 5)$  nm to  $(\frac{\lambda_{Excitation}}{2} + 5)$  nm because the bandwidth of laser is roughly 10 nm. System detection efficiency at different wavelengths is calibrated with standard nonlinear crystal, we use the system detection efficiency to covert measured counts to SHG photon numbers, and then calculate the SHG power. Excitation power at fundamental wavelength is measured with Vega P/N 7Z01560 Power Meter.

#### **ACKNOWLEDGMENTS**

The authors would like to thank the UCSD School of Medicine Microscopy Core for the use of their facility and acknowledge its supporting grant, NS047101. We also would like to thank the Nano3 facility at Calit2 for the use of their facility.

### **Supporting Information**

SHG efficiency calculation, comparison with other double resonance SHG structure, SHG excitation scan curve fitting, SHG enhancement calculation, and simulated radiation

efficiency.

#### References

- (1) Kauranen, M.; Zayats, A. V. Nonlinear Plasmonics. 2012.
- (2) Butet, J.; Brevet, P.-F.; Martin, O. J. F. Optical Second Harmonic Generation in Plasmonic Nanostructures: From Fundamental Principles to Advanced Applications. ACS Nano 2015, 9, 10545–10562.
- (3) Butet, J.; Duboisset, J.; Bachelier, G.; Russier-Antoine, I.; Benichou, E.; Jonin, C.; Brevet, P.-F. Optical Second Harmonic Generation of Single Metallic Nanoparticles Embedded in a Homogeneous Medium. *Nano Lett.* 2010, 10, 1717–1721.
- (4) Zhang, Y.; Grady, N. K.; Ayala-Orozco, C.; Halas, N. J. Three-Dimensional Nanostructures as Highly Efficient Generators of Second Harmonic Light. Nano Lett. 2011, 11, 5519–5523.
- (5) Czaplicki, R.; Husu, H.; Siikanen, R.; Mäkitalo, J.; Kauranen, M.; Laukkanen, J.; Lehtolahti, J.; Kuittinen, M. Enhancement of Second-Harmonic Generation from Metal Nanoparticles by Passive Elements. *Phys. Rev. Lett.* 2013, *110*, 093902.
- (6) Boyd, R. W.; Boyd, R. W. Chapter 1 The Nonlinear Optical Susceptibility. In *Nonlinear Optics*; 2008; pp. 1–67.
- (7) Jha, S. S. Theory of Optical Harmonic Generation at a Metal Surface. *Phys. Rev.* 1965, 140, A2020–A2030.

- (8) Bloembergen, N.; Chang, R. K.; Jha, S. S.; Lee, C. H. Optical Second-Harmonic Generation in Reflection from Media with Inversion Symmetry. *Phys. Rev.* 1968, 174, 813–822.
- (9) Wang, F. X.; Rodríguez, F. J.; Albers, W. M.; Ahorinta, R.; Sipe, J. E.;
  Kauranen, M. Surface and Bulk Contributions to the Second-Order Nonlinear
  Optical Response of a Gold Film. *Phys. Rev. B* **2009**, *80*, 233402.
- (10) Bachelier, G.; Butet, J.; Russier-Antoine, I.; Jonin, C.; Benichou, E.; Brevet, P.-F. Origin of Optical Second-Harmonic Generation in Spherical Gold Nanoparticles: Local Surface and Nonlocal Bulk Contributions. *Phys. Rev. B* 2010, 82, 235403.
- (11) Ciracì, C.; Poutrina, E.; Scalora, M.; Smith, D. R. Second-Harmonic Generation in Metallic Nanoparticles: Clarification of the Role of the Surface. Phys. Rev. B 2012, 86, 115451.
- (12) Pu, Y.; Grange, R.; Hsieh, C.-L.; Psaltis, D. Nonlinear Optical Properties of Core-Shell Nanocavities for Enhanced Second-Harmonic Generation. *Phys. Rev. Lett.* **2010**, *104*, 207402.
- (13) Zhang, Y.; Manjavacas, A.; Hogan, N. J.; Zhou, L.; Ayala-Orozco, C.; Dong, L.; Day, J. K.; Nordlander, P.; Halas, N. J. Toward Surface Plasmon-Enhanced Optical Parametric Amplification (SPOPA) with Engineered Nanoparticles: A Nanoscale Tunable Infrared Source. *Nano Lett.* 2016, 16, 3373–3378.
- (14) Mühlschlegel, P.; Eisler, H.-J.; Martin, O. J. F.; Hecht, B.; Pohl, D. W. Resonant Optical Antennas. *Science (80-.)*. **2005**, *308*.

- (15) Chen, C. K.; Heinz, T. F.; Ricard, D.; Shen, Y. R. Surface-Enhanced Second-Harmonic Generation and Raman Scattering. *Phys. Rev. B* **1983**, *27*, 1965–1979.
- (16) Bouhelier, A.; Beversluis, M.; Hartschuh, A.; Novotny, L. Near-Field Second-Harmonic Generation Induced by Local Field Enhancement. *Phys. Rev. Lett.* 2003, 90, 013903.
- (17) Thyagarajan, K.; Rivier, S.; Lovera, A.; Martin, O. J. F. Enhanced Second-Harmonic Generation from Double Resonant Plasmonic Antennae. *Opt. Express* **2012**, *20*, 12860.
- (18) Linnenbank, H.; Grynko, Y.; Förstner, J.; Linden, S. Second Harmonic Generation Spectroscopy on Hybrid Plasmonic/Dielectric Nanoantennas. *Light Sci. Appl.* **2016**, *5*, e16013.
- (19) Park, S.; Hahn, J. W.; Lee, J. Y. Doubly Resonant Metallic Nanostructure for High Conversion Efficiency of Second Harmonic Generation. *Opt. Express* 2012, 20, 4856.
- (20) Celebrano, M.; Wu, X.; Baselli, M.; Großmann, S.; Biagioni, P.; Locatelli, A.; De Angelis, C.; Cerullo, G.; Osellame, R.; Hecht, B.; et al. Mode Matching in Multiresonant Plasmonic Nanoantennas for Enhanced Second Harmonic Generation. *Nat. Nanotechnol.* 2015, 10, 412–417.
- (21) Yang, K. Y.; Butet, J.; Yan, C.; Bernasconi, G. D.; Martin, O. J. F.
  Enhancement Mechanisms of the Second Harmonic Generation from Double
  Resonant Aluminum Nanostructures. ACS Photonics 2017, 4, 1522–1530.

- (22) Weber, N.; Protte, M.; Walter, F.; Georgi, P.; Zentgraf, T.; Meier, C. Double Resonant Plasmonic Nanoantennas for Efficient Second Harmonic Generation in Zinc Oxide. *Phys. Rev. B* 2017, 95, 205307.
- (23) Harutyunyan, H.; Volpe, G.; Quidant, R.; Novotny, L. Enhancing the Nonlinear Optical Response Using Multifrequency Gold-Nanowire Antennas. *Phys. Rev. Lett.* **2012**, *108*, 217403.
- (24) Aouani, H.; Navarro-Cia, M.; Rahmani, M.; Sidiropoulos, T. P. H.; Hong, M.;
  Oulton, R. F.; Maier, S. A. Multiresonant Broadband Optical Antennas As
  Efficient Tunable Nanosources of Second Harmonic Light. *Nano Lett.* 2012,
  12, 4997–5002.
- Liu, S.-D.; Leong, E. S. P.; Li, G.-C.; Hou, Y.; Deng, J.; Teng, J. H.; Ong, H.
   C.; Lei, D. Y. Polarization-Independent Multiple Fano Resonances in
   Plasmonic Nonamers for Multimode-Matching Enhanced Multiband Second-Harmonic Generation. ACS Nano 2016, 10, 1442–1453.
- (26) Thyagarajan, K.; Butet, J.; Martin, O. J. F. Augmenting Second Harmonic Generation Using Fano Resonances in Plasmonic Systems. *Nano Lett.* 2013, 13, 1847–1851.
- (27) Gennaro, S. D.; Rahmani, M.; Giannini, V.; Aouani, H.; Sidiropoulos, T. P. H.; Navarro-Cía, M.; Maier, S. A.; Oulton, R. F. The Interplay of Symmetry and Scattering Phase in Second Harmonic Generation from Gold Nanoantennas.

  Nano Lett. 2016, 16, 5278–5285.
- (28) Butet, J.; Martin, O. J. F. Fano Resonances in the Nonlinear Optical Response

- of Coupled Plasmonic Nanostructures. Opt. Express 2014, 22, 29693.
- (29) Navarro-Cia, M.; Maier, S. A. Broad-Band Near-Infrared Plasmonic Nanoantennas for Higher Harmonic Generation. ACS Nano 2012, 6, 3537–3544.
- (30) Lyon, L. A.; Pen, D. J.; Natan, M. J. Surface Plasmon Resonance of Au Colloid-Modified Au Films: Particle Size Dependence. 1999, 5826–5831.
- (31) Orendorff, C. J.; Sau, T. K.; Murphy, C. J. Shape-Dependent Plasmon-Resonant Gold Nanoparticles. *Small* **2006**, *2*, 636–639.
- (32) Mock, J. J.; Barbic, M.; Smith, D. R.; Schultz, D. A.; Schultz, S. Shape Effects in Plasmon Resonance of Individual Colloidal Silver Nanoparticles. *J. Chem. Phys.* 2002, 116, 6755–6759.
- (33) Funston, A. M.; Novo, C.; Davis, T. J.; Mulvaney, P. Plasmon Coupling of Gold Nanorods at Short Distances and in Different Geometries. *Nano Lett.* **2009**, *9*, 1651–1658.
- (34) Airola, M.; Liu, Y.; Blair, S. Second-Harmonic Generation from an Array of Sub-Wavelength Metal Apertures. *J. Opt. A* **2005**, *7*, S118–S123.
- (35) Weber, N.; Protte, M.; Walter, F.; Georgi, P.; Zentgraf, T.; Meier, C. Double Resonant Plasmonic Nanoantennas for Efficient Second Harmonic Generation in Zinc Oxide. *Phys. Rev. B* 2017, 95, 205307.
- (36) Lee, J.; Nookala, N.; Gomez-Diaz, J. S.; Tymchenko, M.; Demmerle, F.;

  Boehm, G.; Amann, M.-C.; Alù, A.; Belkin, M. A. Ultrathin Second-Harmonic

  Metasurfaces with Record-High Nonlinear Optical Response. *Adv. Opt. Mater.*

**2016**, 4, 664–670.

- (37) Moreau, A.; Ciracì, C.; Mock, J. J.; Hill, R. T.; Wang, Q.; Wiley, B. J.; Chilkoti, A.; Smith, D. R. Controlled-Reflectance Surfaces with Film-Coupled Colloidal Nanoantennas. *Nature* 2012, 492, 86–89.
- (38) Rozin, M. J.; Rosen, D. A.; Dill, T. J.; Tao, A. R. Colloidal Metasurfaces

  Displaying Near-Ideal and Tunable Light Absorbance in the Infrared. *Nat. Commun.* **2015**, *6*, 7325.
- (39) McLellan, J. M.; Li, Z. Y.; Siekkinen, A. R.; Xia, Y. The SERS Activity of a Supported Ag Nanocube Strongly Depends on Its Orientation Relative to Laser Polarization. *Nano Lett.* 2007, 7, 1013–1017.
- (40) Nicoletti, O.; de la Peña, F.; Leary, R. K.; Holland, D. J.; Ducati, C.; Midgley, P. a. Three-Dimensional Imaging of Localized Surface Plasmon Resonances of Metal Nanoparticles. *Nature* 2013, 502, 80–84.
- (41) Zhou, F.; Li, Z.-Y.; Liu, Y.; Xia, Y. Quantitative Analysis of Dipole and Quadrupole Excitation in the Surface Plasmon Resonance of Metal Nanoparticles. *J. Phys. Chem. C* **2008**, *112*, 20233–20240.
- (42) Dadap, J. I.; Shan, J.; Eisenthal, K. B.; Heinz, T. F. Second-Harmonic Rayleigh Scattering from a Sphere of Centrosymmetric Material. *Phys. Rev. Lett.* 1999, 83, 4045–4048.
- (43) Butet, J.; Bachelier, G.; Russier-Antoine, I.; Jonin, C.; Benichou, E.; Brevet, P.
  F. Interference between Selected Dipoles and Octupoles in the Optical
  Second-Harmonic Generation from Spherical Gold Nanoparticles. *Phys. Rev.*

- Lett. 2010, 105, 1-4.
- Butet, J.; Russier-Antoine, I.; Jonin, C.; Lascoux, N.; Benichou, E.; Brevet, P.
   F. Sensing with Multipolar Second Harmonic Generation from Spherical
   Metallic Nanoparticles. *Nano Lett.* 2012, 12, 1697–1701.
- (45) Sun, Y.; Xia, Y. Shape-Controlled Synthesis of Gold and Silver Nanoparticles. *Sci. (Washington, DC, United States)* **2002**, *298*, 2176–2179.
- (46) Petty, M. C. *Langmuir-Blodgett Films : An Introduction*; Cambridge University Press, 1996.
- (47) Lee, J.; Tymchenko, M.; Argyropoulos, C.; Chen, P.-Y.; Lu, F.; Demmerle, F.; Boehm, G.; Amann, M.-C.; Alù, A.; Belkin, M. A. Giant Nonlinear Response from Plasmonic Metasurfaces Coupled to Intersubband Transitions. *Nature* 2014, *511*, 65–69.
- (48) Dadap, J. I.; Shan, J.; Eisenthal, K. B.; Heinz, T. F. Second-Harmonic Rayleigh Scattering from a Sphere of Centrosymmetric Material. *Phys. Rev.* Lett. 1999, 83, 4045–4048.
- (49) Demichel, O.; Petit, M.; Viarbitskaya, S.; M??jard, R.; De Fornel, F.; Hertz, E.; Billard, F.; Bouhelier, A.; Cluzel, B. Dynamics, Efficiency, and Energy Distribution of Nonlinear Plasmon-Assisted Generation of Hot Carriers. ACS Photonics 2016, 3, 791–795.
- (50) Lassiter, J. B.; Chen, X.; Liu, X.; Ciracì, C.; Hoang, T. B.; Larouche, S.; Oh, S.
   H.; Mikkelsen, M. H.; Smith, D. R. Third-Harmonic Generation Enhancement
   by Film-Coupled Plasmonic Stripe Resonators. ACS Photonics 2014, 1, 1212–

- Mamonov, E. A.; Murzina, T. V.; Kolmychek, I. A.; Maydykovsky, A. I.; Valev,
   V. K.; Silhanek, A. V.; Ponizovskaya, E.; Bratkovsky, A.; Verbiest, T.;
   Moshchalkov, V. V.; et al. Coherent and Incoherent Second Harmonic
   Generation in Planar G-Shaped Nanostructures. Opt. Lett. 2011, 36, 3681.
- (52) Stephan Link, †; Zhong L. Wang, ‡ and; Mostafa A. El-Sayed\*, †. How Does a Gold Nanorod Melt?#. **2000**.
- (53) Tong, L.; Cobley, C. M.; Chen, J.; Xia, Y.; Cheng, J.-X. Bright Three-Photon Luminescence from Gold/Silver Alloyed Nanostructures for Bioimaging with Negligible Photothermal Toxicity. *Angew. Chemie Int. Ed.* 2010, 49, 3485–3488.
- (54) Petrova, H.; Perez Juste, J.; Pastoriza-Santos, I.; Hartland, G. V.; Liz-Marzán, L. M.; Mulvaney, P.; Penisson, J. M.; Bourret, A. On the Temperature Stability of Gold Nanorods: Comparison between Thermal and Ultrafast Laser-Induced Heating. *Phys. Chem. Chem. Phys.* **2006**, *8*, 814–821.
- (55) Ding, S.-J.; Nan, F.; Yang, D.-J.; Zhong, Y.-T.; Hao, Z.-H.; Wang, Q.-Q.
  Tunable Plasmon Resonance and Enhanced Second Harmonic Generation
  and Upconverted Fluorescence of Hemispheric-like Silver Core/Shell Islands.
  Nanoscale 2015, 7, 15798–15805.
- (56) Dill, T. J.; Rozin, M. J.; Palani, S.; Tao, A. R. Colloidal Nanoantennas for Hyperspectral Chemical Mapping. *ACS Nano* **2016**, *10*, 7523–7531.